Supplementary Information

Dirac cone spectroscopy of strongly correlated phases in twisted trilayer graphene

Cheng Shen,[1] Patrick J. Ledwith, [2] Kenji Watanabe,[3] Takashi Taniguchi,[3] Eslam Khalaf, [2] Ashvin Vishwanath, [2] Dmitri K. Efetov[1]

1. ICFO - Institut de Ciencies Fotoniques, The Barcelona Institute of Science and Technology, Castelldefels, Barcelona, 08860, Spain

2. Department of Physics, Harvard University, Cambridge, MA 02138, USA

3. National Institute for Materials Science, 1-1 Namiki, Tsukuba, 305-0044, Japan

A. Methods

Device fabrication.

The whole stacking is fabricated by the van der Waals assembly technique. Graphite, hBN and monolayer graphene flakes are mechanically exfoliated on SiO_2(285nm)/Si^{++} substrates and chosen with optimal thickness by an optical contrast. A few nm thick graphite acting as top gate is first picked up at 100 ℃ by a propylene carbonate (PC) film which is placed on a polydimethyl siloxane (PDMS) stamp. All the other layers are subsequently assembled by repeating this procedure to make the final graphite/hBN/MATTG/hBN/graphite sandwich stacking as we showed in Fig.1a. For the assembling of MATTG, we precut the graphene flake into three separate pieces to reduce strain which is otherwise introduced during the picking up process. The second and third graphene layers are rotated with a target angle around 1.6° and -1.6°, respectively, to achieve the mirror symmetry. The whole stacking is finally released on a SiO_2(285nm)/Si^{++} chip at 180℃ and further patterned into a Hall bar geometry by following a typical ebeam lithography and CHF_3/O_2 reactive ion etching process. Dual gates and Hall bars are edge-contacted with Cr(5nm)/Au(50nm) metal.

Measurements.

The electronic transport measurements are carried out in a dilution fridge and at the base temperature of 35mK unless specified. A standard lock-in technique with excitation frequency f=17.111Hz and ac current <10nA is employed by using Stanford Research SR860. The ac current is applied through 10M ohm resistor. Local top and bottom gate are connected to source meters 2400 to tune carrier density and displacement field. We further apply global gate voltage (10V) to Si/SiO_2 to reduce the resistance of leads that are not gated by local graphite gates. The signals are taken after low-pass RC and LC filters which are used to reduce electron temperature.

Estimation of chemical potential, charge density and twist angle.

Based on the Fermi level location in Nth D-LL and split flat bands, the phase diagram is composed of four types of phases (Extended Data Fig. 1): phase I: Fermi level E_F located inside compressible Nth D-LL and incompressible correlated flat band gap, corresponding to Nth D-LLs crossing with correlated gap as we interpret in main text; phase II: E_F located inside both compressible Nth D-LL and correlated flat band, corresponding to Nth D-LLs crossing with correlated flat band; phase III: E_F located inside incompressible D-LL gap and compressible correlated flat band; phase IV: E_F located inside both incompressible D-LL and correlated flat band gap. Phases I and II host R_{xx} peak as a result of partially filling compressible D-LL. Phase IV hosts quantized R_{xy} plateau. By changing magnetic field, phase IV with $R_{xy} = h/(4N-2)e^2$ transitions to that with $R_{xy} = h/(4N+2)e^2$. This transition corresponds to phase I.

Chemical potential of correlated flat band μ^f with respect to charge filling ν is estimated through phase II following a same method as in ref.[1] When Nth D-LL crosses with flat band, the chemical potential of flat band μ^f relative to Dirac cone vertex equals to $\mu_N^{D-LL} - \mu_{N=0}^{D-LL}$ where $\mu_N^{D-LL} - \mu_{N=0}^{D-LL}$ is chemical potential difference between Nth D-LL and zeroth D-LL that can be extracted experimentally via $\mu_N^{D-LL} - \mu_{N=0}^{D-LL} = v_F\sqrt{2e\hbar Nsgn(N)B}$. Here, v_F is Fermi velocity of Dirac cone, $sgn(N)$ is the sign of LL index $N = 0, \pm1, \pm2, \pm3$ ... and B is perpendicular magnetic field. Charge density in Dirac cone when Nth D-LL is half filled is obtained as $n^D = 4N\frac{B}{\phi_0}$ where $\phi_0 = \frac{h}{e}$ is the flux quantum and factor 4 denotes four-fold spin and valley degeneracy of D-LL. When D-LL is half filled, longitudinal resistance R_{xx} reaches maximum. Hence, band crossing between half-filling D-LLs and flat band is easily recognized with pronounced R_{xx} extrema through which the corresponding magnetic field B can be captured.

We calculated the charge density $n^D \approx 0.5 \times 10^{11} cm^{-2}$ at integer filling $\nu = 2$ and $n^D \approx 1.2 \times 10^{11} cm^{-2}$ at $\nu = 3$ of flat band at zero displacement field. The exact filling of flat band is ν defined by relation $\nu = 4n^f/n_s^f$ (n^f is the charge density of flat band and n_s^f corresponds to full filling of flat band). At lower displacement field D where flat band and Dirac cone coexist, n^f is obtained as $n^f = n^T - n^D$ (n^T is the total carrier density which is acquired through Hall density or gate capacitance). Alternatively, at each filling $\nu = \pm2, 3, \pm4, 5/3, 11/3$, trajectories of Hall plateau or longitudinal resistance R_{xx} minimum (or maximum) with different slopes $\frac{dn}{dB} = (4N + 2)e/h$ converge at zero magnetic field in a $n - B$ space. n^T of the converging point is rightly n^f for these integer or fractional fillings of flat band. At higher displacement field where flat band and Dirac cone are maximally hybridized, n^f is directly obtained as $n^f = n^T$.

To extract the twist angle, we use the relation $n_s^f = 8\theta^2/\sqrt{3}a^2$, where $a = 0.246nm$ is the lattice constant of graphene.

Extraction of correlated gap.

The precise measurement on correlated flat band gap at integer filling relies on precise determination of the crossing points A_N and B_N in $n - B$ phase diagram. In Extended Data Fig. 1, the phase boundary between phase III and IV, or I and II, corresponds to the state of E_F touching split flat band edge, the former of which produces resistive R_{xx} peaks in proximity to integer fillings due to D-LL edge state scattering with unfrozen flat band charges in the edges of split flat band (Fig. 2a), and the latter corresponds to A_N and B_N. In the meanwhile, phase I and phase boundary between III and IV also converge on A_N and B_N. At critical points A_N and B_N, the transition of R_{xy} plateaus with $C = 4N \pm 2$ in magnetic field, which is the characteristic of phase I, disappears. In addition, trajectory of resistive R_{xx} peaks of phase I has a slope of $\frac{dn}{dB} = 4Ne/h$ in $n - B$ phase diagram, but that of phase boundary between III and IV inherits a slope of $\frac{dn}{dB} = (4N - 2)e/h$ from phase IV. This gives rise to a slope transition at A_N and B_N. Notably, as flat band electrons exhibit negative compressibility in proximity to integer fillings, B_N appears at the minimum of magnetic field in $n - B$ phase diagram. Such features help to precisely identify A_N and B_N. Correlated gap is extracted through the as-acquired magnetic field at A_N and B_N. The error of our measurement is determined by the R_{xx} peak and R_{xy} transition width in magnetic field of phase I, which are related to D-LL broadening that is associated with device disorders and magnetic field.

Note that we measure the gap with changed magnetic field. By varying D-LL index, the impacts of magnetic field change on correlated gap can be revealed. At $\nu = 2$ and $D = 0$, when D-LL index changes from $N = 1$ to $N = 2$, magnetic field correspondingly changes from around 0.45T to 0.25T (Fig. 2a). This induces gap decreasing by around 0.5meV, which is much smaller than the extracted correlated gap (see main text). The magnetic field change for correlated gap measurement is around the same order or even less (Fig. 2a). Note due to the Dirac cone shifting in displacement field, at elevated displacement field, phase I appears at a lower magnetic field and thereby the correlated gap would be measured with a bit smaller size. This leads to a slight underestimation of D-induced correlated gap enhancement at $\nu = 2$.

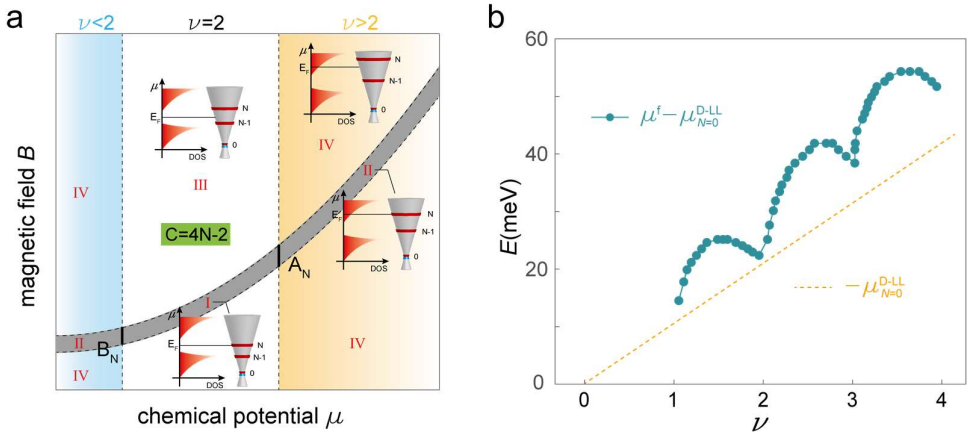

Extended Data Fig. 1 | Phase diagram in perpendicular magnetic field and chemical potential measurement at $D = 0V/nm$. **a**, four types of phases in perpendicular magnetic field when Dirac cone coexists with moiré flat band. The dash lines denote phase boundaries. Phases I and II correspond to partially filling *N*th D-LL, which shows finite band broadening due to disorder effects. The phase boundary between phase I and II is specially marked with solid line, pointing to critical points A_N and B_N as we discussed in main text. For each phase, there is a schematic illustration of filling status at Fermi level E_F for flat band and D-LL. The emergence of correlated gap is shown to arise from flat band splitting. **b**, chemical potential measurement at $D = 0V/nm$. The dark cyan dots show energy difference between flat band and Dirac cone vertex, which is obtained via features of phase II with D-LL index $N = 1$. The yellow dash line denotes a tentative plotting of Dirac cone shifting as a function of charge filling, where the zero energy corresponds to energy of flat band charge neutrality.

B. Correlated states at other fillings

We use our spectroscopy to reveal correlated states of other fillings at zero displacement field. For $\nu = -3$, at high magnetic field where only zeroth D-LL crosses with flat band, the magnitude of Hall resistance R_{xy} is far below $h/2e^2$, indicative of a compressible metallic state (Extended Data Fig. 2). For $\nu = -2$, distinct from $\nu = 2$, R_{xx} showing resistive peak rather than dip, reveals the presence of a few thermal-activated or unlocalized charges at our base temperature (Extended Data Fig. 2), indicating that a tiny or nodal gap is hosted by $\nu = -2$. This conforms to the observed particle-hole asymmetry in MATBG that $\nu = -2$ is usually with a much smaller resistance than $\nu = 2$.[2,3,4]

Fractional filling correlated state between $\nu = 3$ and $\nu = 4$ shows similar features to integer fillings $\nu = 2, 3, 4$ and fractional filling $\nu = 5/3$ with R_{xx} minimum and nearly quantized $R_{xy} = h/[(4N + 2)e^2]$ plateaus (Extended Data Fig. 2 and Extended Data Fig. 3). For high filling where carrier density in Dirac cone can't be ignored, filling ν deviates a lot from the real filling fraction of flat band. We identified $\nu^f = 11/3$ for the real fractional filling of flat band (Extended Data Fig. 3).

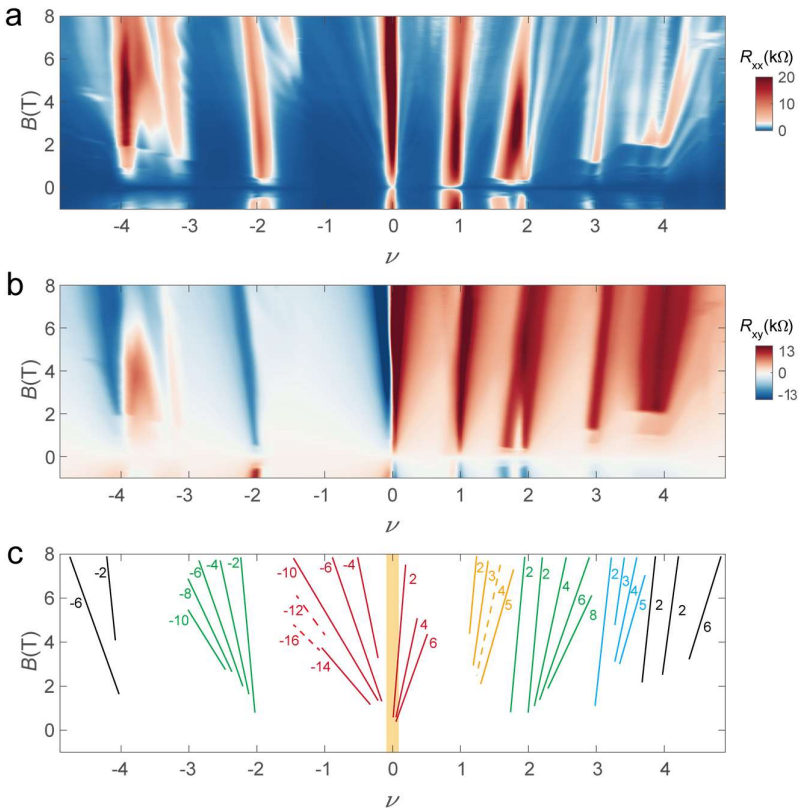

Extended Data Fig. 2 | Landau fan diagram and Landau level crossing at $D = 0V/nm$. **a**, **b**, Landau fan diagram shown by longitudinal resistance R_{xx} and transverse Hall resistance R_{xy}. **c**, schematic of Landau level structure as observed in panel (a) and panel (b).

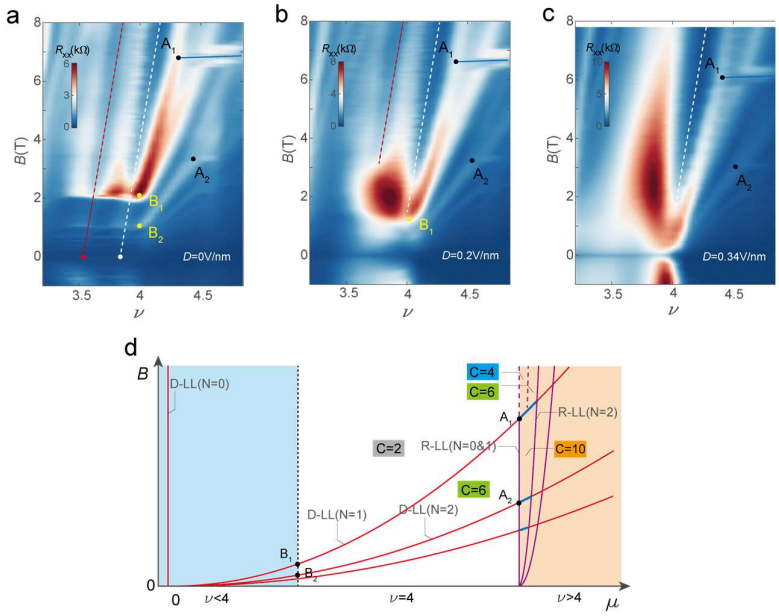

Extended Data Fig. 3 | Correlated states at fractional filling 11/3 and band crossing around $\nu = 4$. **a**, **b**, **c**, Landau fan diagram shown by longitudinal resistance R_{xx} at various displacement field. The dash lines colored red and white trace R_{xx} minimum with $C = 2$ hosted by fractional and full fillings of flat band, respectively. Solid blue lines denote gap closing for the remote band Landau level (R-LL). The ends of dash lines at zero magnetic field, denoted as solid dots, define a total filling ν corresponding to empty filling of Dirac cone, $\nu \approx$

3.53 for red dot, $\nu \approx 3.84$ for white dot. Thus, the real filling fraction of flat band ν^f for this fractional filling state is $\nu^f \approx 4 \times \frac{3.53}{3.84} \approx \frac{11}{3}$. The lower edge of remote band and upper edge of flat band are marked as point 'A' and 'B' with subscript '1' and '2' denoting the D-LL index. Panel (c) is taken at 1.8K. **d**, schematic of band crossing around $\nu = 4$. Red and violet lines represent D-LLs and R-LLs, respectively. Dash violet lines denote symmetry broken R-LLs. The blue lines (corresponding to blue lines in panel (a), (b) and (c)) as one part of the compressible D-LLs here, close the incompressible R-LL gaps.

C. Unchanged v_F in moderate displacement field

We present evidence of little changed v_F of Dirac cone in moderate displacement field which is assumed in the chemical potential and gap extraction with nonzero moderate D. Firstly, in interacting simulations (supplementary section J), we didn't find any signature of reconstruction for Fermi velocity v_F of Dirac cone when moderate displacement field is applied. Secondly, the critical displacement field $D_c(\nu = 2)$ acquired through D-induced R_{xy} transitions at $\nu = 2$ is well consistent with the results of chemical potential which are measured with constant v_F (Fig. 2c).

D. Estimation of $\nu = 4$ single-particle band gap

We use the band crossing method at $\nu = 4$ as depicted for $\nu = 2$. Due to the high energy of remote band edge, the crossing happens at much higher magnetic field than $\nu = 2$, where Landau levels of remote bands (R-LLs) are formed. Crossing between D-LLs and R-LLs induces gap closing for the original incompressible Landau level gaps. Besides the features of band crossing we discussed in main text, tracking the LL gap closing can also help us to determine the exact crossing points A in $\nu - B$ diagram. Via $\mu_A - \mu_{N=0}^{D-LL} = v_F\sqrt{2e\hbar Nsgn(N)B_A}$ and $\mu_B - \mu_{N=0}^{D-LL} = v_F\sqrt{2e\hbar Nsgn(N)B_B}$, we extract at $D = 0$, $\mu_{A,\nu=4} - \mu_{N=0}^{D-LL} = 94.9 \pm 0.7meV$, $\mu_{B,\nu=4} - \mu_{N=0}^{D-LL} = 51.6 \pm 1.8meV$; at $D = 0.2V/nm$, $\mu_{A,\nu=4} - \mu_{N=0}^{D-LL} = 92.6 \pm 0.7meV$, $\mu_{B,\nu=4} - \mu_{N=0}^{D-LL} = 45.7 \pm 2.4meV$; at $D = 0.34V/nm$, $\mu_{A,\nu=4} - \mu_{N=0}^{D-LL} = 89.5 \pm 0.7meV$, with constant $v_F = 10^6 m/s$. It is clear that both $\mu_{A,\nu=4}$ and $\mu_{B,\nu=4}$ decreases with D, signifying split Dirac cone shifting as we discussed in main text.

The most difference of chemical potential measurement at $\nu = 4$ is we need to consider the absent flat band broadening as a consequence of the absent Coulomb interaction energy U' for remote band edge A since Fermi level doesn't reside in correlated flat band any more:

$$\mu_{A,\nu=4}(D) - \mu_{N=0}^{D-LL}(D) = E_0(D) + \Delta_{\nu=4}(D)$$

$$\mu_{B,\nu=4}(D) - \mu_{N=0}^{D-LL}(D) = E_0(D) + U'(D)$$

Here, $\Delta_{\nu=4}$ is single-particle band gap at $\nu = 4$, E_0 is single-particle energy difference from flat band edge to zeroth D-LL. Therefore,

$$\Delta_{\nu=4}(D) = \mu_{A,\nu=4}(D) - \mu_{B,\nu=4}(D) + U'(D)$$

$U'(D)$ is unclear in experiment. Instead, at critical field $D_c(\nu = 4)$, $E_0(D) = 0$ thereby the single-particle gap can be acquired as:

$$\Delta_{\nu=4}(D_c(\nu = 4)) = \mu_{A,\nu=4}(D_c(\nu = 4)) - \mu_{N=0}^{D-LL}(D_c(\nu = 4))$$

With D-LL index $N = 1$ and $D = 0.34V/nm$ which is approximate to $D_c(\nu = 4) \approx 0.37V/nm$, $\Delta_{\nu=4}$ can be obtained around

$$\Delta_{\nu=4}(D_c(\nu = 4)) \approx \mu_{A1,\nu=4}(D = 0.34V/nm) - \mu_{N=0}^{D-LL}(D = 0.34V/nm) = 89.5meV$$

As $\mu_{A,\nu=4}(D_c(\nu = 4))$ is a bit smaller than $\mu_{A1,\nu=4}(D = 0.34V/nm) - \mu_{N=0}^{D-LL}(D = 0.34V/nm)$, $\Delta_{\nu=4}(D_c(\nu = 4))$ should be around but smaller than $89.5meV$.

E. Comparison on transport properties of two neighbor regions

We compare the transport properties of two neighboring regions. R1 is the region between Hall bar A and B where R_{xx} in Fig. 1, Fig.3 and Fig. 4 are acquired, and Fig. 2 goes to R2 that is between B and C. Both of them have a same twist angle of 1.5° and show features of decreased $\mu_A - \mu_{N=0}^{D-LL}$, $\mu_B - \mu_{N=0}^{D-LL}$ and increased $\mu_A - \mu_B$ at $\nu = 2$ in displacement field. The difference is that R2 shows R_{xx} minimum at fractional filling $\nu = 5/3$ rather than R_{xx} maximum as in R1 (Extended Data Fig. 5), hosting a well-developed charge density wave state.

In Extended Data Fig. 4, we show four-probe resistance mapping plot in region R2. It shows a similar displacement field dependence as R1 (Fig. 1c and Fig. 4a).

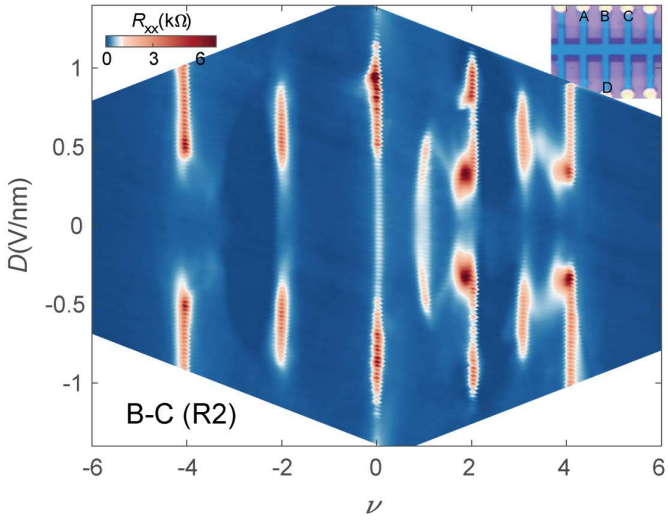

Extended Data Fig. 4 |Additional $R_{xx} - \nu - D$ mapping plot from another part in our device. Four-probe resistance R_{xx} as functions of displacement field D and charge filling ν acquired from Hall bars B-C at zero magnetic field. The inset optical microscopy picture shows measured Hall bars. R_{xy} data throughout this paper are acquired from Hall bars B-D.

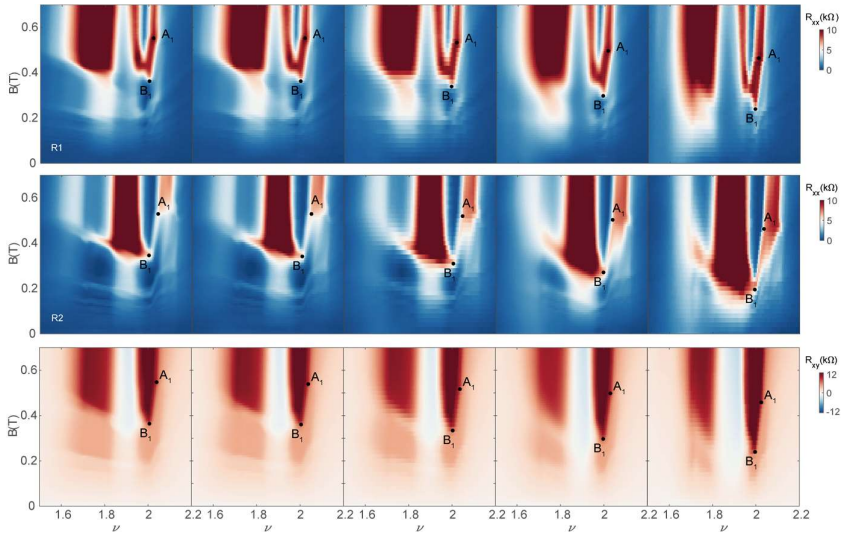

Extended Data Fig. 5 | Zoom-in Landau fan diagram around $\nu = 2$ at a variety of moderate displacement field. The top, middle and bottom panels are mapping plots of longitudinal resistance R_{xx} of two neighbor regions R1 and R2 and Hall resistance R_{xy}, respectively. From the left to the right panel, displacement field D is $D = 0, 0.05, 0.1, 0.15$ and $0.2 V/nm$ in sequence.

F. Hierarchy of correlates states

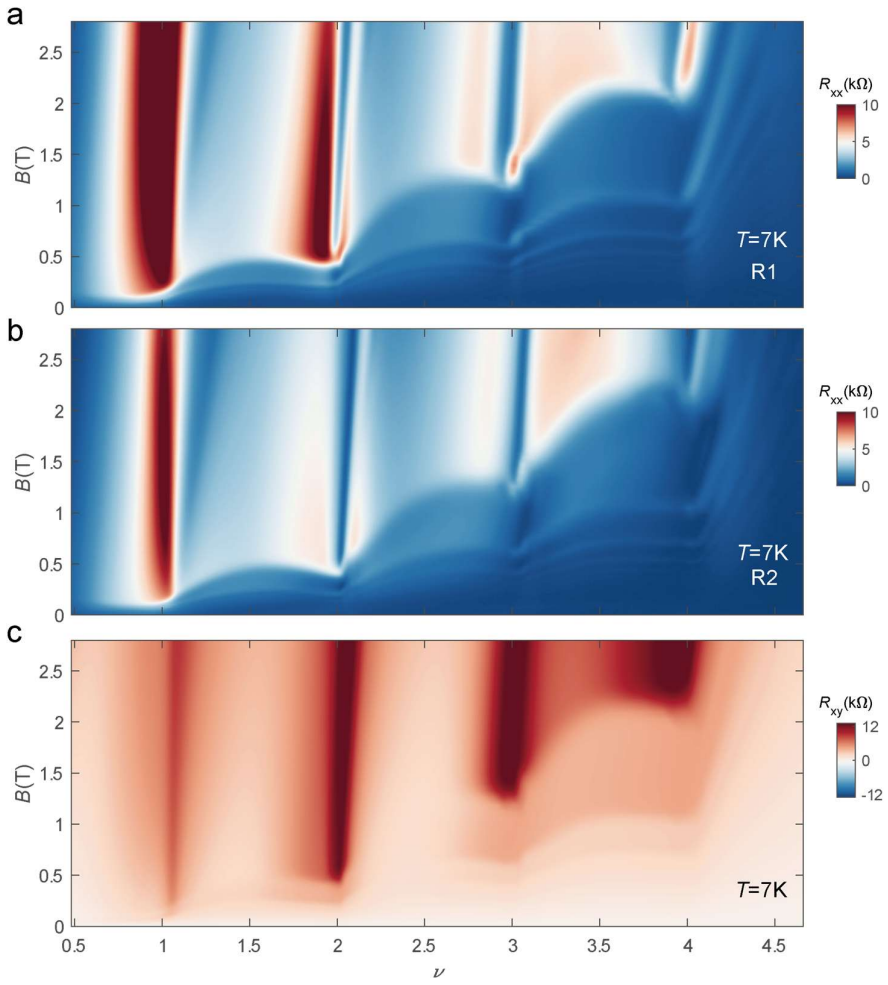

Extended Data Fig. 6 | Hierarchy of correlates states. a-c, longitudinal resistance R_{xx} taken from neighbor region R1 (c), R2 (d) and Hall resistance R_{xy} (e) versus perpendicular magnetic field B and charge filling ν at $D = 0V/nm$ and $T = 7K$. $\nu = 2$ and $\nu = 3$ show robust incompressible gap states, i.e., feature R_{xx} dip and R_{xy} plateaus of $C = 4N + 2$. At $\nu = 1$, R_{xx} peak is favored and R_{xy} deviates from quantized value. There are no signatures of fractional filling $\nu = 5/3$ and $\nu = 11/3$, visualizing the hierarchy of correlated states for various fillings of flat band.

G. Stronger electronic correlation at $D = 0.2V/nm$

At displacement field $D = 0.2V/nm$, most features of Landau fan resemble those at $D = 0V/nm$, i.e., being subject to coexisted non-interacting flat band and Dirac cone. Differences emerge at $\nu = -1$ and $\nu = 2$. As shown in Extended Data Fig. 7, Landau fan originating from $\nu = 2$ exhibits fully lifted degeneracy, distinct from the normal case in MATBG and $D = 0V/nm$ in MATTG where two-fold degeneracy with partial isospin symmetry breaking is favored. At $\nu = -1$, resistive state appears in high magnetic field. These features display much more pronounced spin-valley isospin symmetry breaking, indicative of stronger Coulomb interactions at $D = 0.2V/nm$ as compared to $D = 0V/nm$.

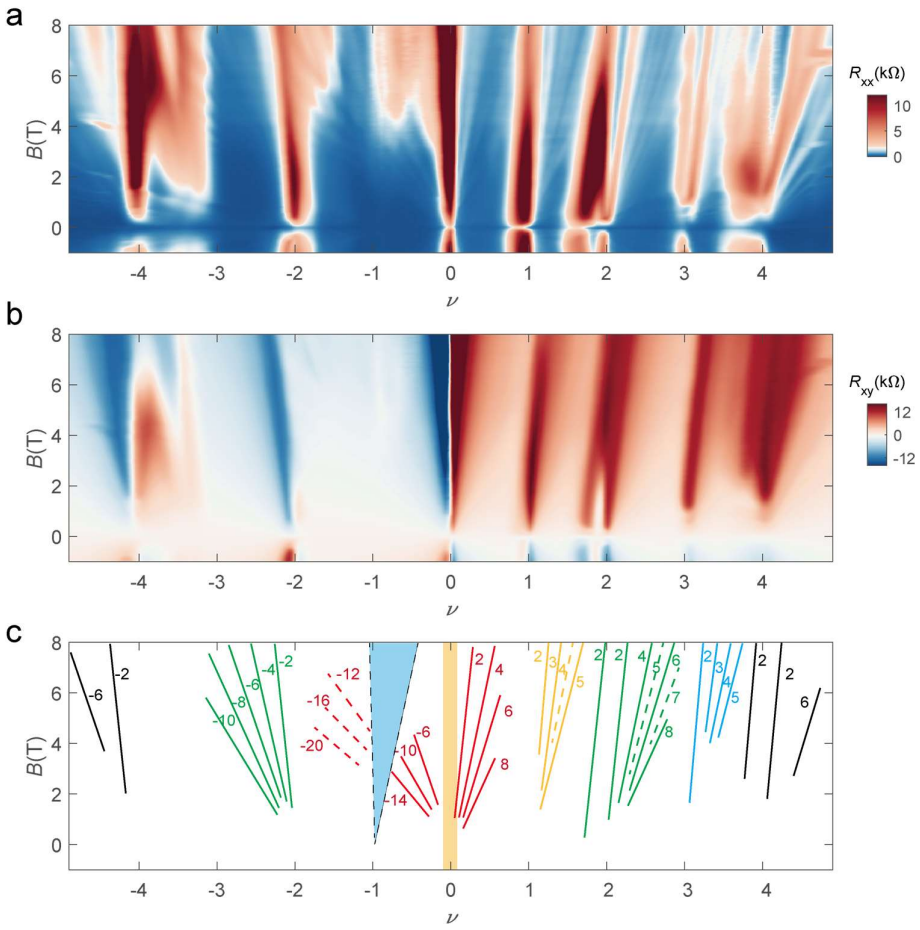

Extended Data Fig. 7 | Landau fan diagram and Landau level crossing at $D = 0.2V/nm$. **a**, **b**, Landau fan diagram shown by longitudinal resistance R_{xx} and transverse Hall resistance R_{xy}. **c**, schematic of Landau level structure as observed in panel (a) and panel (b). The green dash lines denote odd Landau level filling factors from $\nu = 2$. Color shadings around $\nu = 0$ (yellow) and $\nu = -1$ (blue) represent resistive states in magnetic field.

H. Extended temperature-dependent transport data

Extended Data Fig. 8 shows temperature-dependent R_{xx} behavior at a larger temperature scale. At $D = 0.34V/nm$ close to $D_c \approx 0.4V/nm$, transport behavior of MATTG would be mainly dominated by flat band which means phenomena in MATBG will be reproduced in MATTG. For instance, in Extended Data Fig. 8 (a) and (b), Pomeranchuck effect is emergent at $\nu = -1$ with characteristics of vanished R_{xx} peak and increased carrier density for phase boundary of isospin unpolarized states (IU) and symmetry-breaking isospin ferromagnets (IF) at low temperature.

At $D > D_c$, bandwidth W of flat band is remarkably enhanced due to the strong coupling with shifted Dirac cone. The resulted largely reduced correlation strength disables isospin symmetry breaking at $1 < \nu < 2$, which is reflected by the crossed Landau fan from charge neutrality and disappeared resistance peak at $\nu = 1$ for $D = 0.77V/nm$ (Extended Data Fig. 9). Such features of $\nu = 1$ mimic $\nu = -1$ in MATBG.[4] We found $\nu = 1$ at $D = 0.77V/nm$ inherits features of Pomeranchuck effect such as vanished resistance peak at low temperature. The Pomeranchuck state being pronounced at $\nu = 1$ as a result of less strong electronic correlation, conforms to the hierarchy of correlated states for integer fillings of flat band.

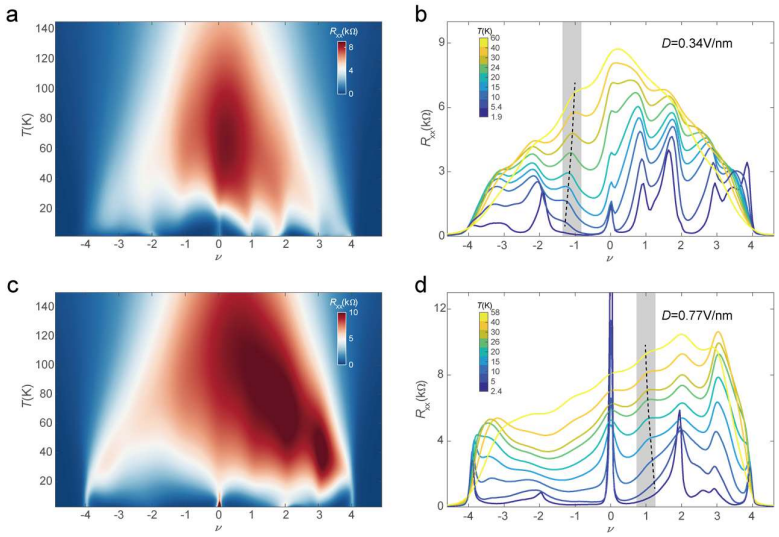

Extended Data Fig. 8| Temperature dependence of four-probe resistance. a, mapping plot of longitudinal resistance R_{xx} as a function of charge filling ν and temperature T at a nonzero displacement field $D = 0.34V/nm$. **b**, linecuts of R_{xx} versus ν taken from panel (a). **c**, **d**, mapping plot and linecuts of R_{xx} at $D = 0.77V/nm$. The gray shadings denote vanishing and shifted R_{xx} peak at low temperature as a signature of Pomeranchuck effect.

I. Overall Landau fan diagram at $D = 0.77V/nm$

At $D = 0.77V/nm$, Dirac cone is fully hybridized and its vertex is split into two, each of which is pushed to the edge of moiré flat band. As a result, Landau level crossing appears only for $|\nu| > 4$ as shown in Extended Data Fig. 9 that Landau fans originating from $|\nu| = 4$ show $C = 4N$ towards charge neutrality whereas $C = 4N + 2$ outwards. Another notable feature of Extended Data Fig. 9 is the response of $|\nu| = 2$ in magnetic field. At $B < 4T$, $|\nu| = 2$ shows Chern number $C = 0$; whereas at $B > 4T$, Chern insulators with $C = 0$ are absent instead replaced by one with $|C| = 2$.

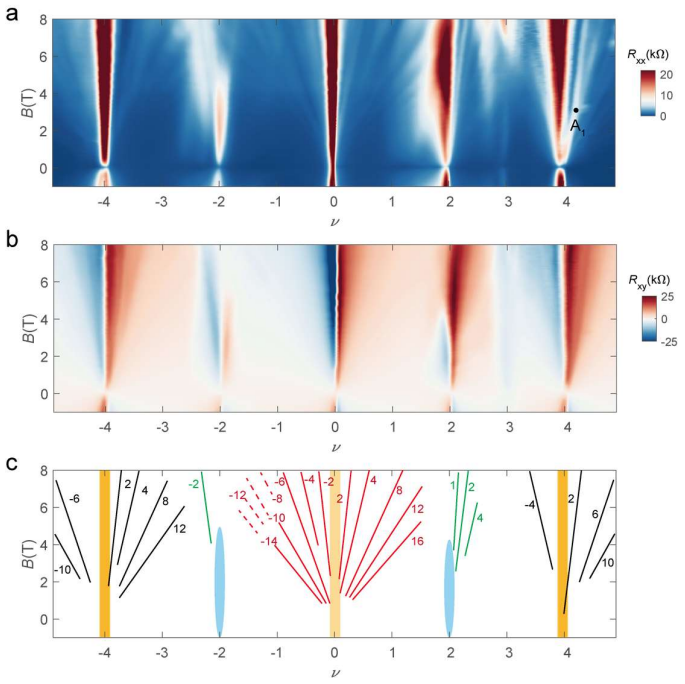

Extended Data Fig. 9| Landau fan diagram and Landau level crossing at $D = 0.77V/nm$. **a**, **b**, Landau fan diagram shown by longitudinal resistance R_{xx} and transverse Hall resistance R_{xy}. **c**, schematic of Landau level structure as observed in panel (a) and panel (b). Landau levels fanning outward from $\nu = \pm 4$ show filling factor sequences of $\nu_{LL} = 4N + 2$, indicating Landau level crossing between Dirac cone and remote dispersive bands, while Landau levels fanning inward from $\nu = \pm 4$ show $\nu_{LL} = 4N$. Resistive states at $\nu = 0$, $\nu = \pm 2$ and $\nu = \pm 4$ are denoted with shadings colored yellow, blue and orange, respectively.

J. Hartree-Fock simulations for MATTG

Twisted trilayer graphene (TTG) at zero displacement field consists of a twisted bilayer graphene subsystem (TBG) as well as a decoupled graphene subsystem. A large body of literature,[5] including analytical[6–9] and numerical[10–17] works, have argued that strainless magic angle TBG is well-described by generalized quantum Hall ferromagnetism in terms of a Chern-band basis. There are eight Chern bands, four of each sign $C = \gamma_z = \pm 1$. Within each Chern sector, the four bands are labeled by their valley $\eta_z = \pm 1$ and spin $s_z = \pm 1$. The quantum Hall ferromagnetic states correspond to fully filling some of these bands, though not necessarily bands with definite valley or spin quantum number – we may take linear combinations within each Chern sector.

At small nonzero displacement fields, these quantum Hall ferromagnets become coupled to the graphene Dirac cones leading to many of the effects described in the main text. Our discussion will summarize results from the detailed perturbation theory carried out in ref. [18](see also ref.[19] which also found a transition from gapless KIVC to gapped VH order). We first focus on spinless TTG at charge neutrality for simplicity. Then we upgrade to $\nu = 2$ TTG which may be thought of as spinless charge neutral TTG on top of a spin polarized background (with an additional Hartree dispersion term).

At zero displacement field, the effective TBG Hamiltonian at charge neutrality is $h_{TBG}(\boldsymbol{k}) = h_x(\boldsymbol{k})\hat{\gamma}_x + h_y(\boldsymbol{k})\hat{\gamma}_y + \hat{\Delta}(\boldsymbol{k})$. Here, $\gamma_{x,y}$ are Pauli matrices that flip the Chern number $C = \gamma_z = \pm 1$ but leave the valley $\eta_z = \pm 1$ invariant. The term $\hat{\Delta}$ is a mean field potential coming the generalized ferromagnetic ordering of the TBG Chern bands; it is proportional to the interaction strength. The two states that we will focus on are the Kramers' intervalley coherent (KIVC) state which is off diagonal in valley, $\hat{\Delta} \propto \gamma_z \eta_{x,y}$, and the valley Hall (VH) state which has $\hat{\Delta} \propto \gamma_z \eta_z$. Both of these states have $\hat{\Delta} \propto \gamma_z$. As a result the mean-field pairing potential anticommutes with the rest of the TBG dispersion for these states; this favors them energetically.[6,7] The charge gap may then be computed as the minimum of

$$2\sqrt{h_x^2(\boldsymbol{k}) + h_y^2(\boldsymbol{k}) + \Delta_0^2(\boldsymbol{k})}$$

over the Brillouin zone, where Δ_0 is the magnitude of $\hat{\Delta}$.

The zero-field graphene Hamiltonian is

$$h_{GRA}(\boldsymbol{k}) = h_{GRA}^{+}(\boldsymbol{k})\hat{\eta}_{+} + h_{GRA}^{-}(\boldsymbol{k})\hat{\eta}_{-}, \quad h^{\pm}(\boldsymbol{k}) = \pm(\boldsymbol{k} - \boldsymbol{K}_{\pm}) \cdot \hat{\boldsymbol{\gamma}},$$

where $\boldsymbol{K}_{+(-)}$ is the momentum moiré K (K') point. Crucially, the Dirac points in different valleys have different moiré crystal momentum. As a result, they cannot develop intervalley coherent order.

The displacement field V induces a tunneling between the two subsystems. Here, we write V to signify the potential difference between the top and bottom layers of MATTG after screening – this is the natural input to theoretical calculations. The relationship between V and the bare, experimental, displacement field D in principle may be obtained through a full self-consistent calculation but here we simply choose an empirical value based on previous studies of moiré systems. We take the conversion factor $V = (0.166\ \text{nm})\, eD$ where $e > 0$ is the magnitude of the electron charge. This is motivated by a comparison between experimental and Hartree Fock studies of twisted monolayer-bilayer graphene where a fractional filling Chern insulator appears for a narrow range of displacement field.[20] Note that ref.[21] used $V = (0.1\ \text{nm})eD$ in the context of twisted double bilayer graphene though this system has four layers.

Turning on a displacement field immediately results in a reconstruction of the non-interacting band structure (see Fig. 1b). The TBG and graphene Dirac cones fully hybridize and lift off of zero energy at the K point, though the system remains gapless due to a Dirac point at the K' point. We emphasize that this effect of the displacement field relies crucially on the lack of a charge gap at the K point in the twisted bilayer graphene subsystem. When the TBG sector has a charge gap, small displacement fields only lead to a small mixing between the TBG and graphene subsystems instead of an immediate, maximal, hybridization. See Extended Data Fig. 1 for Hartree Fock band structures of MATTG with and without a displacement field.

We may understand the effect of the displacement field on states with a TBG charge gap through perturbation theory; we will see that it can be understood in a similar way to the 'superexchange' mechanism in cuprates. The displacement field tunnels TBG electrons to the graphene sector and vice versa. The tunneling is Pauli blocked if the occupations of the subsystems are the same. However, if the occupations are not the same the system may lower its energy by slightly mixing the subsystems. To favor the latter scenario, the displacement field induces a dispersion in both sectors that tries to make the occupations of the two subsystems less similar. In the cuprates, this leads to antiferromagnetism. For us, it is responsible for the increase of the flat band charge gap as well as the transition from the KIVC to a fully gapped VH state at nonzero displacement field as we now describe.

The TBG electrons gain a dispersion $h_V \propto V^2$ which has the opposite sign of the graphene dispersion so that it favors opposite occupation in the two subsystems. This dispersion combines with native TBG dispersion $h_x(\boldsymbol{k})\hat{\gamma}_x + h_y(\boldsymbol{k})\hat{\gamma}_y$ and may increase it or lower it depending on the twist angle. At large twist angles, the TBG dispersion resembles the graphene dispersion, but as the twist angle passes through the magic angle the dispersion changes sign. The angle $\theta = 1.50°$ is expected to be smaller than the angle at which the dispersion changes sign[18] and so we expect the displacement field to effectively increase the native TBG dispersion as we claimed above and in the main text. The increased dispersion will lead to the observed increase in band gap, but it will also increase the "Chern superexchange coupling" $J \propto h^2$ that favors states with $\widehat{\Delta} \propto \gamma_z$. This superexchange coupling is also believed to be responsible for pairing skyrmions, setting the skyrmion effective mass, and setting the critical temperature for the skyrmion superconductor $T_c \propto J$.[7,22,23] The observed increase in T_c with displacement field is consistent with the skyrmion mechanism for superconductivity and increased effective TBG dispersion with displacement field.

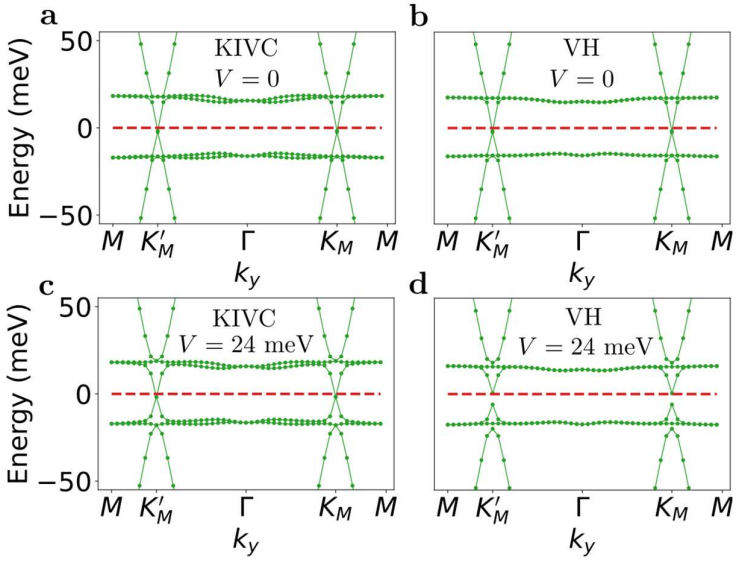

Extended Data Fig. 10 | Self consistent Hartree Fock Band structures for spinless MATTG at charge neutrality. We include band structures for the Kramers' intervalley coherent (KIVC, panels (a) and (c)) and valley Hall (VH, panels (b) and (d)) states at $V = 0$ and $V = 24\ meV$ respectively. Note that the inclusion of both graphene valleys results in graphene Dirac cones at both the K_M and K'_M points. There is no immediate full TBG-graphene hybridization at the K points unlike non-interacting MATTG due to the charge gap in the TBG sector. For the valley Hall state, the graphene Dirac cone gains a mass $m \propto V^2$.

Similarly, the graphene electrons gain a dispersion that is opposite to the TBG dispersion. The TBG dispersion is dominated by the mean-field potential. The induced graphene dispersion was computed in ref.[18] and at the K point is given by

$$m_G = -\frac{V^2|t|^2}{4U}\frac{\widehat{\Delta}}{\Delta_0}.$$

Here, $U \approx 18$ meV comes from the TTG interaction strength and $|t| \approx 0.51$ is a tunneling matrix element that measures the spatial overlap between the TBG and graphene wavefunctions. Recall $\widehat{\Delta} \propto \gamma_z$ for the KIVC and VH states and therefore m_G anticommutes with the graphene dispersion; for these states m_G functions as a Dirac mass that can gap out the graphene subsystem. The KIVC mass can be ignored since as discussed above the graphene Dirac cones are not at the same momentum in each valley. The VH mass term is effective; it generates a gap for the graphene Dirac cones. Because the VH mass term can be energetically satisfied, the energy of the VH state lowers relative to the KIVC state by an amount $\propto m_G^2$. This results in a transition from a KIVC state, where the graphene electrons are semimetallic, to a VH state where the graphene electrons are gapped.[18,19] The transition is dependent on the ratio between intra-sublattice tunneling and inter-sublattice tunneling κ, which is largely unknown. Ref.[18] estimates $\kappa = 0.58$ and a critical displacement field of $V = 100$ meV or $D \approx 0.6$ V/nm.

We now comment on generalizing these results to $\nu = 2$. At $\nu = 2$, we may describe candidate ferromagnets with total Chern number zero by polarizing the same two flavors in each Chern sector and then half filling the remaining four bands. The flavor polarization is expected to correspond to a spin polarization, as valley polarization breaks time reversal symmetry which seems unlikely due to the proximate superconductors. The spin polarization may be aligned or anti-aligned in the two valleys depending on the sign of the intervalley Hunds coupling[22] but this does not matter for our purposes and we assume aligned spins in both valleys; one may always rotate the spin in the other valley to translate our conclusions to the spin-valley locked case. With this assumption, one spin is completely polarized, let's call this spin "down". The unpolarized, up, spin sector resembles charge neutral twisted bilayer graphene, though with the additional background charge density from the down spins.

The background charge induces a mostly flavor diagonal Hartree dispersion $h_0(k)$ for the TBG electrons which has a prominent dip at the Γ point (see ref.[24] for a detailed discussion). Because the Hartree dispersion is largely flavor diagonal, it simply adds onto the previously discussed spinless charge neutral TBG dispersion $\pm\sqrt{h_x^2(\boldsymbol{k}) + h_y^2(\boldsymbol{k}) + \Delta_0^2(\boldsymbol{k})}$. Near the magic angle, the Hartree dip causes the conduction band to have a minimum at the Γ point. The valence band maximum is very parameter dependent because the charge neutral TBG dispersion and the Hartree dip usually nearly cancel which results in a very flat band. The maximum may be at the Γ point but even if it is not the valence band is flat enough that the energy at the Γ point is a good approximation. Thus, up to a constant determined by the Hartree dip, we approximate the charge gap for $\nu = 2$ with the charge neutrality band gap at the Γ point of spinless TTG. Accordingly, we performed Hartree-Fock simulations for charge neutral spinless TTG and extracted the change in the band gap at the Γ point as a function of V; this is plotted in Extended Data Fig. 11. It is worth noting that, within Hartree Fock theory and with perfect spin polarization, only spin up electrons acquire the mass m_G in the flat band VH state; the spin down electrons remain semimetallic. However, to our knowledge there is no symmetry that protects the gaplessness of the spin down electrons because C_2T has been broken by the VH order. Thus there may be beyond-Hartree-Fock effects that lead to a small gap amongst the spin down electrons. We leave a microscopic calculation of the resulting spin down gap to future work. Note that the activated gap and resistance peak for $\nu = 2$ is much smaller than that of $\nu = 0$ (see Fig. 4a).

At zero displacement field, the background charge density from the polarized down spin simply shifts all of the graphene Dirac cones up in energy. However, by the same argument given above for the graphene mass, when a nonzero displacement field is turned on the system wants the down spin graphene electrons to be unoccupied so that displacement-field induced tunneling is not Pauli-blocked. This effect acts to shift the down spin graphene Dirac cones further up in energy, relative to zero displacement field. The additional shift is given by

$$\mu_{\downarrow} = \frac{|t|^2 V^2}{4U}.$$

Note that the experimental gap extraction assumes that the Dirac cones are not spin split. The above splitting can therefore lead to an underestimate of the gap increase with displacement field (see Extended Data Fig. 11). It also leads to the observed decrease in $\mu_B - \mu_{N=0}^{D-LL}$ (Fig. 2c).

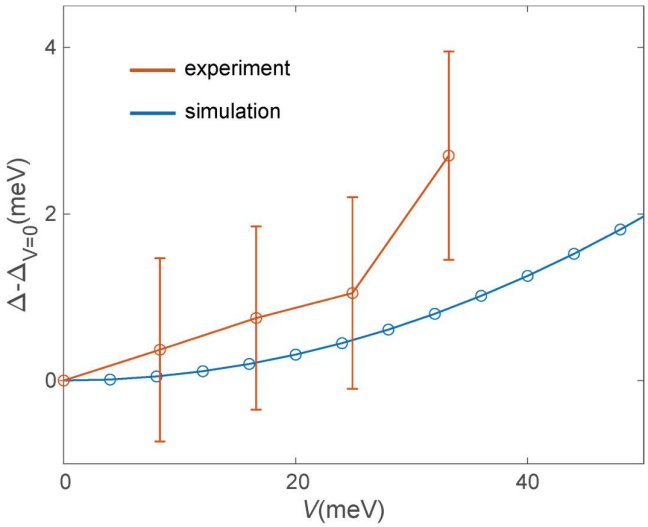

Extended Data Fig. 11 | Gap enhancement at $\nu = 2$ with respect to displacement field D. The blue line denotes gap enhancement for $\nu = 2$ approximated with charge neutrality band gap at the Γ point of spinless TTG which is calculated with Hartree-Fock simulations. The orange line presents results extracted experimentally. Here, we use $V = (0.166\ \text{nm})\, eD$ to convert displacement field D to potential difference V between top and bottom layers of TTG.

We now comment on the observed fractional filling state at $\nu = 5/3$. Our approach is to consider a Hartree Fock band structure at $\nu = 2$ and look for van Hove singularities upon hole-doping the valence bands. For simplicity, and motivated by an ignorance of other small scales that may change the order of the valence bands, we neglect the bare dispersion which enables us to do Hartree Fock without iterating for self-consistency. In this limit there are two valence bands that are each three-fold degeneracy. Because the valence bands are quite flat, we assume that the interaction will spontaneously choose one valence band to hole dope by 1/3 and thus ignore the degeneracy. Remarkably, we find that the top valence band at hole filling 1/3 is extremely close to a van Hove singularity where six hole pockets surrounding the Γ point merge into a single annular fermi sea. Furthermore, the annular Fermi sea is very close to being nested with respect to the six wavevectors $\left(R_{2\pi/6}\right)^m Q_1$. Here, $m = 0,1,2,3,4,5$; $Q_1 = k_\theta(0,-1)$ is a vector connecting the two moiré K points; and $R_{2\pi/6}$ is a rotation by $2\pi/6$. These vectors are precisely the translation breaking wavevectors that correspond to a $\sqrt{3} \times \sqrt{3}$ tripling of the unit cell. We therefore conclude that one third hole filling the top valence band – and spontaneously lifting the approximate three-fold degeneracy – puts the system in a state that is highly unstable to tripling the unit cell. This matches experimental observations of an insulating state at this filling that is related to a van Hove singularity.

References

1. Park, J. M., Cao, Y., Watanabe, K., Taniguchi, T. & Jarillo-Herrero, P. Tunable strongly coupled superconductivity in magic-angle twisted trilayer graphene. *Nature* **590**, 249–255 (2021).
2. Yankowitz, M. *et al.* Tuning superconductivity in twisted bilayer graphene. *Science* **363**, 1059–1064 (2019).
3. Liu, X. *et al.* Tuning electron correlation in magic-angle twisted bilayer graphene using Coulomb screening. *Science* **371**, 1261-1265 (2021).
4. Saito, Y. *et al.* Isospin Pomeranchuk effect in twisted bilayer graphene. *Nature* **592**, 220–224 (2021).
5. Ledwith, P. J., Khalaf, E. & Vishwanath, A. Strong Coupling Theory of Magic-Angle Graphene: A Pedagogical Introduction. *arXiv Prepr. arXiv2105.08858* (2021).
6. Bultinck, N. *et al.* Ground State and Hidden Symmetry of Magic-Angle Graphene at Even Integer Filling. *Phys. Rev. X* **10**, 31034 (2020).
7. Khalaf, E., Chatterjee, S., Bultinck, N., Zaletel, M. P. & Vishwanath, A. Charged skyrmions and topological origin of superconductivity in magic-angle graphene. *Sci. Adv.* **7**, 5299 (2021).
8. Bernevig, B. A., Song, Z.-D., Regnault, N. & Lian, B. Twisted bilayer graphene. III. Interacting Hamiltonian and exact symmetries. *Phys. Rev. B* **103**, 205413 (2021).
9. Lian, B. *et al.* Twisted bilayer graphene. IV. Exact insulator ground states and phase diagram. *Phys. Rev. B* **103**, 205414 (2021).
10. Xie, M. & MacDonald, A. H. Nature of the correlated insulator states in twisted bilayer graphene. *Phys. Rev. Lett.* **124**, 97601 (2020).
11. Liu, S., Khalaf, E., Lee, J. Y. & Vishwanath, A. Nematic topological semimetal and insulator in magic-angle bilayer graphene at charge neutrality. *Phys. Rev. Res.* **3**, 13033 (2021).
12. Cea, T. & Guinea, F. Band structure and insulating states driven by coulomb interaction in twisted bilayer graphene. *Phys. Rev. B* **102**, 45107 (2020).
13. Soejima, T., Parker, D. E., Bultinck, N., Hauschild, J. & Zaletel, M. P. Efficient simulation of moiré materials using the density matrix renormalization group. *Phys. Rev. B* **102**, 205111 (2020).
14. Parker, D. E., Soejima, T., Hauschild, J., Zaletel, M. P. & Bultinck, N. Strain-induced quantum phase transitions in magic-angle graphene. *Phys. Rev. Lett.* **127**, 27601 (2021).
15. Kang, J. & Vafek, O. Non-Abelian Dirac node braiding and near-degeneracy of correlated phases at odd integer filling in magic-angle twisted bilayer graphene. *Phys. Rev. B* **102**, 35161 (2020).
16. Potasz, P., Xie, M. & MacDonald, A. H. Exact diagonalization for magic-angle twisted bilayer graphene. *arXiv Prepr. arXiv2102.02256* (2021).
17. Xie, F. *et al.* Twisted bilayer graphene. VI. An exact diagonalization study at nonzero integer filling. *Phys. Rev. B* **103**, 205416 (2021).
18. Ledwith, P. J. *et al.* TB or not TB? Contrasting properties of twisted bilayer graphene and the alternating twist $ n $-layer structures ($ n= 3, 4, 5,\dots $). *arXiv Prepr. arXiv2111.11060* (2021).
19. Christos, M., Sachdev, S. & Scheurer, M. S. Correlated insulators, semimetals, and superconductivity in twisted trilayer graphene. *arXiv Prepr. arXiv2106.02063* (2021).
20. Polshyn, H. *et al.* Topological charge density waves at half-integer filling of a moiré superlattice. *Nat. Phys.* **18**, 42–47 (2022).
21. Liu, X. *et al.* Tunable spin-polarized correlated states in twisted double bilayer graphene. *Nature* **583**, 221–225 (2020).
22. Chatterjee, S., Bultinck, N. & Zaletel, M. P. Symmetry breaking and skyrmionic transport in twisted bilayer graphene. *Phys. Rev. B* **101**, 165141 (2020).
23. Chatterjee, S., Ippoliti, M. & Zaletel, M. P. Skyrmion superconductivity: DMRG evidence for a topological route to superconductivity. *arXiv Prepr. arXiv2010.01144* (2020).
24. Parker, D. *et al.* Field-tuned and zero-field fractional Chern insulators in magic angle graphene. *arXiv Prepr. arXiv2112.13837* (2021).